LA-UR-14-22709
Approved for public release; distribution is unlimited.

Title: Neutron Diffraction Measurement of Residual Stresses, Dislocation Density and Texture in Zr-bonded U-10Mo “Mini” Fuel Foils and Plates

Author(s): Brown, Donald W.
Okuniewski, M.A.
Sisneros, Thomas A.
Clausen, Bjorn
Moore, G.A.
Balogh, L

Intended for: Report

Issued: 2014-08-07 (rev.2)

# Neutron Diffraction Measurement of Residual Stresses, Dislocation Density and Texture in Zr-bonded U-10Mo "Mini" Fuel Foils and Plates

**D.W. Brown[1], M. A. Okuniewski[2], T. A. Sisneros[1], B. Clausen[1], G. A. Moore[2], L. Balogh[3]**

[1]Los Alamos National Laboratory, Los Alamos, New Mexico, 87545

[2]Idaho National Laboratory, Idaho Falls, Idaho 83415

[3]Queens University, Kingston, Ontario

## Abstract

Aluminum clad monolithic uranium 10 weight percent molybdenum (U-10Mo) fuel plates are being considered for conversion of several research and test nuclear reactors from high-enriched to low-enriched uranium fuel due to the inherently high density of fissile material. Comprehensive neutron diffraction measurements of the evolution of the textures, residual phase stresses, and dislocation densities in the individual phases of the mini-foils throughout several processing steps and following hot-isostatic pressing to the Al cladding, have been completed. Recovery and recrystallization of the bare U-10Mo fuel foil, as indicated by the dislocation density and texture, are observed depending on the state of the material prior to annealing and the duration and temperature of the annealing process. In general, the HIP procedure significantly reduces the dislocation density, but the final state of the clad plate, both texture and dislocation density, depends strongly on the final processing step of the fuel foil. In contrast, the residual stresses in the clad fuel plate do not depend strongly on the final processing step of the bare foil prior to HIP boding. Rather, the residual stresses are dominated by the thermal expansion mismatch of the constituent materials of the fuel plate.

## Introduction

In support of the United States' nonproliferation and highly enriched uranium (HEU) minimization policies, the U.S. Department of Energy (DOE)/National Nuclear Security Administration's (NNSA) Global Threat Reduction Initiative (GTRI) is actively working to convert civilian research and test reactors from the use of HEU fuel to low enriched uranium (LEU) fuel [1]. GTRI's Reactor Conversion program provides governments and facilities around the world with technical and economic assistance for conversion. If no suitable LEU fuels are available, the program contributes to the development of new LEU fuels. To date, GTRI has converted or verified the shutdown of 87 research reactors worldwide, including 20 domestic facilities. Of the remaining domestic research reactors, five U.S. high performance research reactors (USHPRRs) and one associated critical assembly will require a new high density LEU fuel and fabrication capability, which is currently under development, to convert.

Existing qualified fuels do not meet the high fuel density requirements for the operation of these high-performance reactors, which include the Advanced Test Reactor (ATR) at Idaho National Laboratory, the High Flux Isotope Reactor (HFIR) at Oak Ridge National Laboratory, the University of Missouri Research Reactor (MURR), the Massachusetts Institute of Technology Reactor (MITR), and the Department of Commerce's National Bureau of Standards Reactor

(NBSR). To maintain performance requirements, the Reactor Conversion program is developing a high density monolithic plate fuel system which uses low enriched uranium 10wt% molybdenum (U-10Mo) foils clad with Al [2, 3]. A thin (~0.025 mm) zirconium inter-diffusion barrier layer on the U-10Mo foil prevents the formation of U-Al intermetallics, the properties of which may be detrimental to the fuel performance [1, 2, 4].

Several processing steps, including a hot co-rolling step to bond the Zr to the U-10Mo foil, a post-hot-roll (PHR) anneal, cold-rolling, and final post-cold-roll (PCR) anneal are considered prior to the final hot isostatic pressing (HIP'ing) of the fuel foil to the Al cladding. Clearly, the microstructures of each phase evolve throughout the different processing steps and the final microstructure can potentially be manipulated through understanding and control of the processing parameters. Also, due to the difference in the coefficients of thermal expansion (CTE) of the fuel, cladding, and diffusion barrier materials and differential plasticity, unique residual stress states will develop in the fuel plates dependent on the final processing step.

Microstructural studies of as-processed clad monolithic fuel foils are to be found in the literature but tend to focus on phases formed at the interfaces [4-6] or residual stresses between the fuel, diffusion prevention layer, and cladding [7-9]. Previous high energy X-ray diffraction studies report a strong in-plane compressive stress in the U-10Mo foil in a clad fuel plane and observed a significant reduction of dislocation density following the HIP bonding step [9]. The current work presents a comprehensive neutron diffraction study of the evolution of the textures, residual phase stresses, and dislocation densities in the individual phases of the fuel foils throughout several processing steps and the fuel plate (following HIP bonding).

## Experimental Details

### *Sample Preparation*

Several fuel foils were fabricated at Idaho National Laboratory (INL) to distinct final processing steps [10]. Table 1 lists the foils by identification number and describes the processing. Depleted uranium and molybdenum feedstock were arc-melted in an inert atmosphere and cast into a 2.5 mm thick coupon and homogenized. 99.8% pure Zr foil, 0.25mm thick, was procured from Goodfellow in a rolled and annealed state. The zirconium diffusion barrier was co-rolled (hot-rolled) onto the U-10Mo fuel foil at 923K. Each foil received the hot-rolling step, but the amount of hot rolling varied from 81% to 90.5% such that the final thickness of each foil, including the Zr diffusion barrier, was 0.25mm (see Table 1 for details). The rolling schedule consisted of three 10%-reduction passes, three 7% reduction passes, three 6%-reduction passes, and the remaining passes at 5% until the desired thickness was achieved. This is essentially the starting state for the foils in this study and was coined sample 490-1. Foils then received a post-hot-roll (PHR) anneal at 923K for 45 minutes (492-2) followed by distinct cold-rolling steps to 20% (493-1) or 50% (482-1) reduction. Following 50% cold-rolling, several foils were given a post-cold-roll (PCR) anneals at 923K (485-1), 1023K (485-2), or 1123K (486-1) or 60 minutes. The final dimensions of the foils were nominally 19mm wide by 82mm long by 0.25mm thick.

Diffraction patterns were collected from the "bare" foils (comprised of U-10Mo fuel and Zr diffusion barrier) to determine residual stress, texture and dislocation density. The samples were then returned to INL and clad with Al by hot-isostatic pressing (HIP'ing) [2, 3, 11]. A recess which loosely fit the U-10Mo foil was machined into one side of the aluminum cladding, thus

the cladding is thinner on one side of the foil. Six fuel plates of U-10Mo foil and aluminum cladding were stacked vertically with graphite parting layers and tool steel strong backs separating each sample [2]. The samples were heated to the HIP'ing temperature of 560ºC at 4.8ºC/min after which 104 MPa of pressure was applied during the 90 minute soak time. Subsequently, the HIP assembly was cooled at ~4.8ºC/min to room temperature. Following HIP'ing, the final dimensions of the mini-plates were 150 mm x 50 mm x 1.5 mm. The aluminum cladding was then sheared to the final dimensions of the plate, 101.4 mm x 25.25 mm x 1.5 mm. The fuel foil maintained the same dimensions, but was not centered in the cladding. On one end (the end monitored), the edge of the fuel foil was only 4.7 mm from the edge of the plate, while on the other it was 18.7 mm from the edge of the plate. Following the cladding step, diffraction data were collected again on the same samples to monitor the evolution of the microstructure.

Due to limited beam time and availability of some samples, not all foils were measured and re-measured to the same degree. For instance, the 1123K PCR annealed foil was not measured after cladding.

*Neutron Diffraction Measurement*

The diffraction geometry is shown schematically in figure 1. The neutron diffraction measurements were completed on the SMARTS diffractometer at LANSCE [12]. SMARTS accepts a pulsed "white" neutron beam (continuous wavelength spectrum from 0.5Å - 4.0Å) from a 283K water moderator located roughly 31m from the sample position. The neutrons are scattered from the illuminated portion of the sample (called the "gauge volume") and collected in two fixed angle detector banks situated at $\pm 90^{\circ}$ (+ Bank 1, – Bank 2) from the incident beam each defining a unique diffraction vector ±135° from the incident neutron beam and normal to each other. Recently, a third detector bank (Bank 3) has been incorporated at SMARTS below the incident beam at a scattering angle of 148°, providing a high resolution option for quantitative diffraction line profile analysis (DLPA).

The incident neutron beam was defined using computer controlled, motorized, boron-nitride slits and impinged on the sample. The slit size was controlled with respect to the purpose of each individual measurement. During spatially resolved strain profiling, the slits were set to 2mm in the direction of the profile and 5mm in the direction transverse to the profile to reach a compromise between spatial resolution and count time. Likewise, for measurements aimed at collecting data on the very thin Zr layer, the slits were opened to 5mm x 5mm, to optimize for counting statistics while sacrificing spatial resolution. Finally, in order to quantitatively determine dislocation density and crystallite size, high statistics runs were completed on the hot-rolled, 20% cold-rolled, and 50% cold-rolled bare foils which were assumed to have the most defected microstructures. The incident beam was enlarged to 10 mm tall by 15 mm wide and three 0.25 mm thick bare foils were stacked to increase counting statistics. Count times of roughly four hours yielded high statistical quality data in the backscattering detector bank (Bank 3) suitable for quantitative DLPA.

Multiples samples were mounted simultaneously on purpose designed fixtures which were rigidly mounted to the SMARTS diffractometer sample translation table and located with respect to the diffractometer center through the use of computer controlled theodolytes [12]. The samples were oriented such that one in-plane direction, longitudinal (L) or transverse (T), and the

normal (N) direction were aligned with each diffraction vector simultaneously providing two distinct diffraction patterns probing different sample directions. The samples were translated with respect to the beam to record diffraction patterns as a function of position in each of the samples. The samples were then re-oriented and diffraction patterns collected such that the diffraction vectors probed the other in-plane direction and provided a repeat measurement in the normal direction.

In typical neutron diffraction measurements of residual stress on a white beam source, the detector view is focused using radial collimators [13-16] defining the gauge volume in the third dimension. This practice both provides depth resolution as well as ensures that the gauge volume does not move with respect to the diffractometer during profiling resulting in large fictitious strain observations [17]. However, due to the thin foil nature of these samples, that practice was not possible (while retaining reasonable count times) and diffraction data was collected from the entire thickness of the samples.

Thus, there is no through-thickness resolution in these measurements. The samples studied herein, especially the U-10Mo foil and Zr diffusion barrier, are very thin relative to their in-plane directions and little through-thickness variation of stresses is expected, but the reader should remain cognizant that the collected diffraction patterns represent an average through the thickness of the sample. Finite element models of the HIP process show little through-thickness variation of the stress in the Al cladding [18], but these do not attempt to include the rolling procedure, which is known to impart strong through-thickness stress gradients [19].

Further, because the gauge volume is not defined in three dimensions, small shifts of the samples from the diffractometer center with the motion of the translator table, which are almost inevitable because the samples were not perfectly straight, will result in fictitious strains. This effect can be large compared to mechanical strains [17] and is generally avoided at all cost. This was anticipated, and an on-board calibrant in the form of an annealed thin copper foil (0.07 mm) was attached symmetrically to each face of the samples to detect and correct the fictitious strains. Annealed copper was chosen because the diffraction peaks from copper do not interfere with those of Al, U-10Mo, or Zr and because, in the annealed state, the strength of the copper is very low, limiting the potential residual stresses in the “calibrant”, thus limiting the possible errors from assuming it is stress free. Finally, the foils were very thin and copper has low thermal neutron absorption, maximizing the number of neutrons that reach the sample and, subsequently, the detector.

While this procedure provides a good calibration of the two detector banks against each other (to be demonstrated below) and between the several samples probed, it should not be considered an absolute calibration. Absolute calibration, to the accuracy required for lattice strain measurement, is extremely difficult to achieve. Because the beam penetrates into the bulk of the sample, the calibrant would not only have to be verified stress free, but would also have to have the same geometry as well as neutron scattering and absorption cross sections as the sample. Otherwise, the “center of diffraction” is effectively shifted because scattering from the gauge volume is not evenly distributed, but weighted by both absorption and scattering strength. This again results in fictitious strains.

Validation of the calibration was attained for free, so to speak, by rotating the sample 90° about a vertical axis when re-orienting from the T/N lattice parameter measurement to the L/N. This

results in the two N lattice parameter determinations occurring in the opposing banks and will provide a strong validation of the calibration procedure for the mini-foil and plate measurements.

The current method of using an on-board calibrant symmetrically placed on each side of the sample allows us to accurately compare lattice parameters determined along multiple sample directions, in this case, the N, L, and T directions. The difference in lattice parameter in the three directions is directly related to the deviatoric strain and stress tensors but, without further assumption, is insensitive to an arbitrary hydrostatic stress. However, due to the thinness of the sample, it is reasonable to assume that the out of plane stress components are zero far from any boundaries, i.e. at the center of the sample. This assumption, in turn, fixes the arbitrary hydrostatic stress component at the sample center.

*Data analysis* Whole pattern Rietveld refinements of the diffraction patterns were accomplished using the GSAS software developed at Los Alamos National Laboratory [20] using TOF profile 1 [21]. The data was analyzed to determine the crystallographic texture, the lattice parameters which are used to calculate residual stress, and peak variances of each phase which are related to the dislocation density.

*Texture* Time-of-Flight (TOF) neutron diffraction is ideal for determining a specific projection of the orientation distribution function, that is the inverse pole figure (IPF) [22]. The IPF is a plot of pole density as a function of crystal orientation (hkl) along a specific sample direction, e.g. the N direction, on an irreducible sterograph [23]. This is precisely what is measured on a TOF diffractometer with fixed detector banks, that is with the diffraction vector aligned with a specified sample direction, e.g. the N direction. The pole densities are determined with GSAS using a spherical harmonic expansion of the orientation distribution function [24]. The coefficients of the spherical harmonics are determined by fitting the observed peak intensities to those calculated. The multiplicative correction factors for the preferred orientation in the Rietveld refinement are precisely the Multiples of Random Distribution (MRD) plotted on the irreducible stereograph to produce IPFs [25].

*Residual Stress* The lattice parameter, *a*, was determined at each measurement position *(x,y)* and the elastic lattice strain determined from $\varepsilon(x,y) = \frac{a(x,y) - a_0}{a_0}$ (eq.1), where $a_0$ represents a reference, stress-free, lattice [parameter. The uncertainty in the lattice parameter measurement, ~0.0001Å (relative uncertainty, corresponding to a strain uncertainty of ~0.00003 or 30με), is determined from the estimated standard deviation in the fit to the lattice parameter. Thus, it represents statistical uncertainty and ignores systematic uncertainty which may result, for instance, from misalignment of the sample or assumptions of the reference lattice parameter.

Acceptable reference samples were not available for the aluminum or the U-10Mo because it was not possible to fabricate a reference sample without sending it through the identical thermo-mechanical procedures. For instance, it is known that the Mo content changes during the HIP'ing procedure as α-U precipitates [9, 26]. The reference lattice parameters of the U-10Mo and Al were determined by forcing the normal component of the stress ($\sigma_{33}$) to zero near the center of

the plate, far from any boundary. Specifically, the average normal component of the stress determined at measurement points more than 20 mm from the end of the fuel was forced to zero. Note, this is the same assumption used to fix the normal stress component to zero at the center of the plate and does not add any additional uncertainty to apply again at this point. This point will be discussed in more detail below.

The residual strains are determined in three orthogonal directions, N, L, and T. The residual stresses in the same directions are then determined from Hooke's law:

$$\sigma_L = \frac{E}{1+\nu}\left\{\varepsilon_L + \left[\frac{\nu}{1-2\nu}\left(\varepsilon_L + \varepsilon_T + \varepsilon_N\right)\right]\right\} \text{ (eq.2) [27]},$$

where we have used E = 70 GPa and ν = 0.33 for the aluminum and E = 86 GPa and ν = 0.35 for U-10Mo [28-30]. The indices can be rotated as necessary to solve for the remaining stress components.

Determining residual stresses in the Zr diffusion prevention layer is more difficult. The crystallographic texture of the Zr diffusion barrier is such that only the **c** lattice parameter can be determined with sufficient accuracy in the N direction and the **a** lattice parameter in the L and T directions. Thus, the lattice parameters cannot simply be compared in multiple sample directions as done for the U-10Mo and the Al to find the deviatoric stress components. However, the $c_N/a_L$ and $c_N/a_T$ ratios can be calculated with a great deal of accuracy (±0.0005). Taking the ratio of the lattice parameters removes issues with absolute calibration, and the experimentally determined ratio can be compared to that found in literature for pure Zr to get an indication of the stress state of the diffusion barrier.

Because the **c** and **a** axes are normal to each other, the specified ratios characterize two distinct grain sets that actually exist in the diffusion barrier, that is **c**||N and a||L or a||T. Moreover, because these orientations represent the dominant grain orientation in the Zr, thermal residual stresses due to the anisotropic thermal expansion of Zr should be minimal in these grains [31, 32].

While a quantitative determination of the residual stresses in the Zr layer will not be possible from the current data, the stresses in the barrier can be estimated as follows. The stress state of the Zr diffusion prevention layer is approximated as in-plane equi-biaxial, that is $\sigma_N = 0$ and $\sigma_L = \sigma_T$, resulting in the simplification $\varepsilon_L = \varepsilon_T = \frac{1-\nu}{E}\sigma_L$ (eq. 3) and $\varepsilon_N = \frac{-2\nu}{E}\sigma_L$ (eq. 4). In the dominant grain orientation, i.e. **c**-axis parallel to N and **a**-axes parallel to L (or T), the strain components can be written as $\varepsilon_N = \frac{c - c_0}{c_0}$ or $c = c_0\left(1 + \varepsilon_N\right)$, where $c_0$ is the reference lattice parameter and c the lattice parameter under conditions of stress. The same relation can be written between the **a** lattice parameter and the L and T strains. The $\frac{c_N}{a_L}$ ratio at stress can then be

written $\frac{c_N}{a_L} = \frac{c_0(1+\varepsilon_N)}{a_0(1+\varepsilon_L)}$ (eq 5). Substituting equations 3 and 4 into equation 5 and solving for $\sigma_L$, the longitudinal stress component can be estimated as $\sigma_L = \frac{E\left(1-\frac{c_N/a_L}{c_0/a_0}\right)}{(1-\nu)\left(\frac{c_N/a_L}{c_0/a_0}+2\nu\right)}$ (eq 6).

Using a representative literature value of $\frac{c_0}{a_0} = 1.5928$ [33-35], and appropriate elastic properties for Zr (E=100GPa and n=0.3 [36]) the in-plane component of the residual stress can be estimated from eq. 6. Note, this estimation assumes isotropic elastic properties of Zr, which is not a good approximation and the assumption of equi-biaxial stress is also suspect, but they are sufficient to get an estimate of the residual stress.

*Dislocation Density*

Information about the microstructure can be gleaned from the diffraction peak breadth or variance, which is determined by the Rietveld refinements in GSAS. The diffraction peak variance is frequently assumed to be a sum of contributions from the strain distribution associated with dislocations ($\varepsilon_{rms}$ or "microstrain"), and finite coherent crystallite domain (sub-grain) size, although other microstructural effects can also increase the peak breadth. The broadening due to $\varepsilon_{rms}$ can be separated from that due to finite crystal size through the d-space (or momentum transfer, q, alternatively) dependence of the broadening [37, 38] [21] if data of sufficient quality (count statistics and instrumental resolution) is collected and several peaks are analyzed. The instrumental resolution in the ±90 detector banks on SMARTS is generally not sufficient for quantitative DLPA. In the context of this work, we will interpret the peak breadth as indicative of dislocation density, as discussed in past work [9]. Without going into detail, the $\sigma_1$ profile parameter incorporated in the GSAS TOF profile function 1 [21] is related to the root mean square strain, $\varepsilon_{rms} = \sqrt{\langle \varepsilon^2 \rangle} = \frac{1}{C}\sqrt{8\ln 2\left(\sigma_1^{\,2} - \sigma_i^{\,2}\right)}$ [21], where C is the diffractometer constant determined from the instrumental calibration and $\sigma_i$ is the instrumental broadening, determined in this case from the scattering from the annealed copper foil.

We will use the mean square strain determined for each of the fuel foils in the ±90° banks as only a qualitative indicator of dislocation density. In the case of a dislocated crystal, $\varepsilon_{rms}$ depends on the size of the integration distance used to calculate the mean [38-40]. For the purpose of qualitative assessments, this dependence can be neglected and it can be assumed with tolerable accuracy that the $\varepsilon_{rms}$ is proportional to the dislocation density [41-43].

Additionally, high resolution data was collected on the high-angle bank with sufficient counting statistics to enable quantitative DLPA on three samples assumed to have the highest dislocation density, i.e. the hot-rolled, 20% cold-rolled, and 50% cold-rolled samples. These data sets were analyzed for dislocation density and finite crystal size using the extended Convolutional Multiple Whole Profile (eCMWP) line profile analysis method [44]. The methodology of the employed diffraction line profile analysis procedure is the following: theoretical profile functions are calculated as the convolution of the theoretical size, strain (dislocation) and planar fault profiles and measured instrumental profiles which have as parameters the characteristics of the microstructure. These theoretical profiles are based on physical models, which describe the effect of size, dislocations and faulting on the shape of the diffraction profiles [45]. The theoretical profile functions are fitted to the full measured pattern by a non-linear least-squares algorithm and thus the parameters of the microstructure, for example the dislocation density, are determined [44]. The instrumental profile was determined from the on-board annealed copper calibrant.

**Results**

*Diffraction patterns* Figure 2 shows sections of diffraction patterns collected on the hot-rolled, 50% cold-rolled and 923K PCR annealed bare foils. Each was collected in detector bank 2 with the sample oriented such that the diffraction vector was parallel to the sample L direction. The U-10Mo (110), (200), and (211) peaks are highlighted as well as the Zr (110) peak. The FWHM of each peak is indicated, where appropriate, by the dotted lines.

It is clear that the relative peak intensities change as a function of processing step, indicating texture evolution. The U-10Mo (110) peak is strongest in the hot-rolled sample, while the (200) peak is strongest in the annealed sample. The peak breadth also significantly depends on the processing step. The 50% cold-rolled sample exhibits markedly broader diffraction peaks than the hot-rolled sample with the peaks from the annealed sample being narrowest of all. The shifts in lattice parameter due to residual strain are typically too small to identify in a diffraction pattern with the naked eye.

Little variation of the Zr (110) peak is observed between the three samples. Clearly, the intensity of the Zr (110) peak is unchanged. It is possible that the Zr (110) peak from the cold-rolled sample is broader than the others, but the statistical quality of the data does not allow detailed analysis of the Zr line broadening.

*Texture* The Al cladding shows little preferred crystallographic orientation and its texture will not be shown here for brevity. Figures 3a-h show the Zr N direction IPF's in the (3a.) as-received (prior to bonding to the Al cladding) state and following the processing steps described in Table 1. As, received, the Zr texture is moderately strong, peak of ~4 Multiples of Random Distribution (MRD) with the basal pole predominantly aligned with the rolling normal direction. The prism poles, (10.0) and (11.0), are isotropically distributed in the plane of the foil (IPF's not shown). Following hot-rolling (3b.), the Zr texture increases in strength to ~6 MRD. Following hot-rolling, the variations in the texture of the Zr layer (Fig. 3b-h) are not significant relative to

the measurement uncertainty. Further, no significant change in the textures of the Zr diffusion prevention layer are observed following HIP bonding of the fuel foil to the aluminum cladding (not shown).

Figures 4a-g show all three IPF's (N, L, and T) representing the U-10Mo fuel texture as a function of the processing step. In contrast to the Zr layer, considerable texture evolution is evident in the U-10Mo foil with each successive processing step. Following hot-rolling, a typical bcc rolling texture is evident, with (110) poles aligned with the rolling direction and (111) poles along the foil normal [23]. The texture is weakened somewhat, from a peak of 5.2 MRD to 4.0 MRD following the PHR anneal at 923K for 45 minutes. Cold-rolling to 20% or 50% once again increases the strength of the texture to a peak of 4.4 MRD. In contrast to the PHR anneal, the PCR anneal at 923K for 60 minutes almost completely randomizes the texture. Indeed, following the higher temperature anneals at 1023K and 1123K, a distinct texture component develops with the (100) poles aligned with the rolling direction.

Again for brevity, figures 5a-g show only the N direction IPF's of the U-10Mo foils following the HIP bonding to the aluminum cladding. No texture evolution is observed following bonding. In fact, the reproducibility of the IPF's is striking given the simplicity of the technique and analysis.

*Lattice parameters* The relative cross-calibration of lattice parameter measurement in the two 90° detector banks with the on-board annealed Cu foil calibrant and its implications for measurements of residual stress has been discussed in detail in a previous publication [46]. Figures 6a-c show the lattice parameters of the U-10Mo and Al along the distinct sample directions (N, L, and T) determined along the centerline of the hot-rolled foil as a function of distance from the edge of the U-10Mo foil. Figures 6a and b show the lattice parameters of the U-10Mo bare foil and after cladding, respectively, and have the same scale. Figure 6c shows the lattice parameters of the Al following cladding. The edges of the U-10Mo foil and Al plate are indicated by dashed and solid vertical lines, respectively. The center of the U-10Mo foil is at 41 mm. At negative distances, the neutron beam probes only Al in the mini-plate, off the edge of the U-10Mo foil. The scale of all three plots is such that full scale represents a strain of 0.0047 (4700 $\mu\varepsilon$); a fractional lattice parameter change equivalent to 200 $\mu\varepsilon$ is indicated on each figure.

Figures 7a-c and 8a-c show similar data collected on the 50% cold-rolled foil and the 923K, PCR annealed foil. The plots are shown in order of processing and the scales are consistent. Similar data was collected on all 7 samples, but these three effectively represent the observations. The agreement in absolute lattice parameter between the samples (all 7, not just the 3 shown here) is striking and effectively validates the calibration procedure.

In the bare foils, the repeat measurements of the N direction lattice parameters were completed in the same bank, Bank 1, and did not significantly differ. In contrast, the Al clad plates were rotated between the L and T lattice parameter measurements such that the repeat N measurements occurred in distinct banks, in order to check the relative calibration of the two ±90° banks against each other. In this case, both measurements of the N lattice parameter are shown. The agreement between the two measurements is on the edge of the statistical uncertainty in the lattice parameter obtained from the peak fitting and systematic. The N lattice parameter is consistently slightly smaller when measured with the sample horizontal and the N direction in bank 1, then when the sample was vertical and the N direction in bank 2. In all

cases, the average of the two measurements of the lattice parameters in the sample normal direction is used to calculate strains and stresses.

The lattice parameters are obviously direction dependent in each of the samples; the difference is much larger than the uncertainty or the disparity between the repeat measurements of the normal lattice parameter. The variation is indicative of deviatoric stress components. The nature of the dependence is unique to each sample. In the bare foils, the variation in lattice parameters correspond to a few hundred microstrain, and is very dependent on the final processing step, specifically, whether the last step is mechanical in nature, or thermal. In both the hot-rolled and 50% cold-rolled samples (Fig. 6a and 7a), the lattice parameters in the N and T direction are large relative to the L (rolling) direction. In the annealed bare foils (Fig 8a.), the trend is distinct; the L and T lattice parameters are significantly larger than the N lattice parameter. Little significant spatial variation in the lattice parameters is observed in any of the bare foil samples with the relatively poor spatial resolution of the neutron diffraction measurements.

Following cladding, the direction dependence of the lattice parameters is much larger, but is relatively independent of the final processing step of the bare foil prior to cladding. In each case, at the center of the foil (41 mm) the lattice parameter in the N direction is relatively large, in the L direction small, and the T direction intermediate. The difference between the N and L directions corresponds to a roughly 2000 με. Moreover, the lattice parameters in each unique sample direction in the three foils are relatively close in an absolute sense. This is true over all samples measured.

Also, there is a clear spatial variation of the U-10Mo lattice parameters in the clad samples, which is again independent of the final processing step of the bare foil prior to cladding. The N lattice parameter exhibits little significant evolution with distance from the edge of the foil while the L lattice parameter initially increases as the edge as approached, and then sharply decreases within 5 mm of the edge. The T direction lattice parameter decreases monotonically as the edge of the foil is approached.

The lattice parameters in the aluminum cladding exhibit variation of the opposite sense, although considerably reduced. The L and T lattice parameters in the cladding are generally larger than the N lattice parameter, although the L and N parameters trend together at the center of each sample. All three lattice parameters tend to the same value, 4.0505Å, as the edge of the Al plate, at -4.6 mm, is approached.

Figures 9a and b show the c/a ratio (c in the N direction, a in the L and T directions) in the Zr diffusion barrier layer as a function of the final processing step, including the as-received annealed Zr, in the (a.) bare foils and after (b.) subsequent cladding. These measurements were at the center of the foil. The literature value [33-35] is also indicated. Both measurements of the c/a ratio in the reference Zr are within uncertainty of each other and the accepted literature value. While the uncertainties are large due to the small amount of Zr in the beam, once the Zr is co-rolled and bonded to the U-10Mo foil, the c/a ratios are consistently larger than in the as-received Zr; either $c_N$ is too large, or $a_L$ and $a_T$ are too small, or both. Following the 50% cold-roll step, the c/a ratios increase roughly linearly with increased annealing temperature. Following cladding, the c/a ratios remain larger than in the reference Zr, but exhibit little systematic dependence on the state of the foil prior to cladding.

*Residual Stress* While the residual stress in the bonded Zr layer cannot be determined quantitatively from the current data, it can be estimated from eq. 6. There is little apparent evolution of the c/a ratio, and presumably residual stress in the Zr diffusion barrier, between hot-rolled, PHR annealed, 50% cold-rolled, and the 923 PCR annealed foils, but the c/a ratio increases monotonically as the PCR anneal temperature is increased. The largest c/a ratio of 1.5995 observed in the foil annealed to 1123K corresponds to an estimated compressive residual stress of roughly -320 MPa. The lower c/a ratios near 1.5950 correspond to roughly -100 MPa. Following cladding, little systematic variation of the c/a ratio of the Zr layer with the final processing step of the bare foil is observed. A c/a ratio of 1.5960, near the center of the scattered data, corresponds to an estimated residual stress of ~-150 MPa.

Little spatial variation was observed in the lattice parameters in bare U-10Mo foils (on the length scale observable by neutron diffraction), see figures 6-8, and the spatially varying residual stresses in both the Al and U-10Mo of the clad fuel foils has been discussed elsewhere [9,Brown, 2014 #1943]. The stress profiles observed from these particular plates are similar to the previous reports. Thus, the remainder of this paper will focus on the process dependent microstructural evolution at the center position in each foil. Figure 10a shows the N, L, and T components of the residual stress in the U-10Mo determined at the in-plane center of each bare foil as a function of the final processing step, in order of occurrence. Figure 10b and c show the residual stress components in the fuel foil and Al cladding following HIP bonding of the cladding to the fuel foil.

The magnitudes of the stresses in the U-10Mo in the bare foils are not large relative to the strength of the material [8, 29], never reaching an absolute value greater than 100 MPa. The thermal annealing steps drive the U-10Mo in-plane stresses (L and T) in the bare foil toward tension. Considering only the three PCR annealed foils, i.e. foils with the same starting state, the in-plane residual stresses increase monotonically with the annealing temperature. The residual stress in the L direction increases faster with temperature than in the T direction. In contrast, the cold-rolling steps consistently drive the in-plane stresses in the U-10Mo foil into compression, more strongly in the L direction (rolling direction) than the T direction.

Following HIP bonding of the Al cladding to the U-10Mo fuel foil, the stresses in both the foil and the cladding are relatively independent of the final processing step of the foil prior to cladding. Consistent with previous measurements [9], the L component of the residual stress is the largest at roughly -150MPa and the T component is between -50MPa and -100MPa. The in-plane residual stresses in the Al cladding are tensile and are also larger in the L direction, but limited to less than 50MPa.

Figure 10c includes an inset (shaded) which shows the reference lattice parameter, d0, determined for the Al cladding by forcing the normal stress to be zero. The variation of the reference lattice parameter amongst the six samples is less than the statistical uncertainty in determining the Al lattice parameters from an individual diffraction pattern. This was not forced and provides further confidence in the atypical calibration of the instrument and the assumptions inherent in calculating the residual stresses. It is not expected that the reference lattice parameter of the U-10Mo foil would be constant throughout processing because each thermal step raises the temperature through the nose of the TTT curve [29], holds the material at a temperature where the Mo is stable in solution, and then slowly cools through the chemically unstable region. Thus,

it is expected that the dissolved Mo content, and thus the reference lattice parameter will be a complicated function of the thermal profile of each step [26].

*Peak Widths*

The evolution of peak width is apparent in the diffraction pattern to the naked eye in figure 2. Figure 11 shows a conventional Williamson-Hall (WH) plot [37] of the peak breadths ($\Delta q$) as a function of momentum transfer ($q = 2\pi/d$) collected on the high resolution bank (Bank 3) on SMARTS. Data are shown from the hot-rolled, 20% cold rolled, and 50% cold-rolled bare foils. The instrumental width has been taken to be that from the reference annealed copper foil and has been interpolated to the q positions of the U-10Mo peaks. Qualitatively, the slopes of the lines on the conventional WH plot are related to the dislocation density, the y-intercept to the coherent crystal domain size [38].

The instrumental resolution, of order $\Delta q/q \sim 0.03\%$, is nearly insignificant as it is ~5x narrower than the peaks from the foils. The broadening observed by eye in the diffraction peaks (figure 2) is quantified in the WH plot. The peaks get broader going from the hot-rolled sample, to 20% cold-rolled, to 50% cold-rolled. More specifically, between the hot-rolling and 20% cold-rolling steps, the slope of the WH plot increases. Recall, there is a PHR anneal to 923K between hot-rolling and cold-rolling processing steps. In contrast, between the 20% cold-rolling and 50% cold-rolling steps, the slope remains constant, but the y-intercept increases.

Figure 12 shows the root mean square strain, $\varepsilon_{rms}$, as a function of the final processing step of the bare foil before and after cladding. We assume $\varepsilon_{rms}$ is directly related to the dislocation density, but will not quantitatively determine the dislocation density from that data. Two measurements are shown in each condition (except 20% cold rolled), with the sample horizontal and vertical; the results are within uncertainty. The dislocation density of the material clearly evolves with each processing step. Following hot-rolling a significant dislocation population exists in the foil. The subsequent PHR anneal at 923K for 45 minutes decreases the dislocation density, but does not take it to the minimum value observed, i.e. it is not within uncertainty of zero. The dislocation density increases monotonically with 20% and 50% cold-rolling. The PCR anneal at 923K for 1 hour reduces the dislocation density to a value lower than the PHR anneal at similar conditions. The PCR anneal to 1023K reduces the dislocation density to a slightly lower value. Increasing the annealing temperature to 1123K does not further reduce the dislocation density, within our uncertainty.

The root mean square strain was determined from the Rietveld refinement performed on diffraction patterns collected from each sample, but does not provide quantitative information. Changes in crystal domain size are convoluted in those results. Diffraction data sufficient for quantitative DLPA were collected on only select samples due to time limitations. Table 2 shows quantitative values of the dislocation density and average crystal domain size in the three worked foils (hot-rolled, 20% and 50% cold-rolled) determined from DLPA on high statistical quality data collected on the high resolution detector bank. Following hot-rolling, which bonds the Zr layer to the U-10Mo foil, a significant dislocation density of $(11 \pm 4)\ x10^{14}/m^2$ remains in the U-10Mo foil. The foil is then annealed at 923K for 45 minutes which presumably (figure 12) reduces the dislocation density significantly. Rolling to 20% reduction of thickness again increases the dislocation density to a very high value of $(43 \pm 4)\ x10^{14}/m^2$, but the coherent crystal domain size has not changed significantly. Further rolling to 50% reduction does not

increase the dislocation density significantly, but does reduce the crystallite size from greater than 50 nm to roughly 30nm.

**Discussion**

*Microstructural Evolution During Processing* The results presented above show clear evolution of diffraction patterns from bare U-10Mo fuel foils as a function of processing steps and following HIP bonding of an Al cladding. The change in diffraction patterns can be interpreted as microstructural evolution and a clear picture throughout the thermal and mechanical processing of the foils and plates is obtained.

The Zr diffusion barrier is bonded to the U-10Mo during the initial hot-rolling process and this is the starting microstructure for this study. The hot-rolling step is unique in this study in that it comprises both thermal and mechanical processes, and this is reflected in the residual stress. Following the hot rolling step, the U-10Mo is in compression in the L direction, and stress free in the N and T directions. Despite the high temperature (923K), a significant dislocation density is present following hot-rolling, indicating that dynamic recovery was not complete. Also, a strong crystallographic texture with (110) poles in the rolling direction, typical of rolled bcc materials [23], exists following hot-rolling. Finally, the texture of the Zr diffusion barrier strengthened considerably during hot-rolling.

The subsequent 923K, 45 minute PHR anneal drives the in-plane residual stresses toward tension roughly an equal amount and weakens the texture. The dislocation density is also reduced during the heat treatment, but not to zero. Clearly recovery is active during the PHR anneal, but we will momentarily argue it is not complete.

The two rolling steps, 20% and 50% thickness reduction, drive the L residual stresses in the U-10Mo foil into compression (more so with each step) while the T component remains close to zero. The rolling texture strengthens and the dislocation density increases with rolling, as expected. Rolling to 20% reduction appears to mainly increase the dislocation density, while increasing the reduction from 20% to 50% only decreases the crystal domain size, that is the sub-grain size in the U-10Mo.

The observed residual stresses in the rolled foils must be considered carefully. The residual stress that results from the differential plasticity between the Zr and U-10Mo that occurs during cold-rolling is more complicated than simple temperature changes and likely requires detailed finite element analysis to understand. Moreover, rolling likely imparts significant through-thickness variation in the residual stress state [19] and the current diffraction measurements have no through-thickness resolution. Also, the stresses in the U-10Mo and Zr do not obviously provide stress balance as they are both compressive. It is possible that stress balance is provided by a tensile stress at another position in the foils. However, little spatial variation of the stress in the U-10Mo was observed given the spatial resolution of the technique. The stress in the Zr was not determined at positions other than the center.

The PCR anneal of the 50% cold-rolled foil to 923K for 1 hour resulted in an equi-biaxial, in-plane tensile residual stress of 40±10MPa in the U-10Mo foil. In this case, stress balance is plausibly achieved as the in-plane stresses in the Zr diffusion barrier were roughly -150 MPa. Following this anneal, $\varepsilon_{rms}$ is near the minimum value observed, indicating that the dislocation

density is very low, i.e. the material effectively recovered. The near complete randomization of the texture following the 923K PCR anneal indicates that recrystallization, and thus certainly recovery [47], has occurred during the heat treatment. We can assume then that the residual stress was completely annealed out at temperature, and the stress following cooling is due solely to the CTE mismatch between the U-10Mo and Zr. The U-10Mo ($\alpha_{U\text{-}10Mo} = 11.8x10^{-6}$/K [8]) foil contracts more during cooling than the Zr diffusion barrier ($\alpha_{Zr} = 5.7x10^{-6}$/K, **a**-direction [31]) foil. If edge effects are ignored, then one expects an equi-biaxial in-plane tensile stress state in the U-10Mo, and balancing compression in the Zr, as observed.

The higher temperature PCR annealing treatments (1023K and 1123K) reduce the dislocation density marginally more than the 923K PCR anneal. Also, a new texture component with (100) poles parallel to the original rolling direction develops during the higher temperature anneals, more so at 1123K. Finally, the higher temperature anneals drive the in-plane residual stresses further into tension, but do not maintain the in-plane symmetry. Specifically, the T residual stress increases at a slower rate with increasing temperature than does the L stress. The increase in residual stress with increasing annealing temperature indicates that the annealing is not instantaneous. That is, the hold time at 923K is necessary to relax the stress, whereas passing through 923K while cooling from the 1123K anneal does not relax the stresses that have built up during cooling from the higher temperature anneal. Also, following cooling from 1023K and 1123K, the stress state is no longer equi-biaxial; the transverse stress is relaxed relative to the longitudinal. This must be because of the proximity of the transverse edge, only 9.5 mm from the center of the foil relative to the longitudinal edge, 41 mm away. The lesser constraint in the transverse direction results in increased relaxation in the transverse direction (relative to the longitudinal direction) during cooling when the residual stress is larger, that is when the temperature change is larger.

It is interesting to compare the response of the U-10Mo to the 923K PHR and PCR anneals given that the conditions for the thermal treatments were very similar, only different in time, 45 minutes and 60 minutes, respectively. The PHR anneal resulted in a larger remnant dislocation density following the heat treatment and exhibited little texture randomization, whereas the PCR anneal resulted in near complete randomization that one would associate with recrystallization. It seems likely that the difference in the outcome between the PHR and PCR anneals must be the microstructure of the material prior to the anneal. The dislocation density, which is indicative of stored energy in the microstructure, following hot-rolling is four times less than that following the cold-rolling. The increased stored energy in the microstructure following cold-rolling drives the recovery and recrystallization [47]. In contrast, much less energy is stored in the microstructure following hot-rolling, and the drive to fully recover and recrystallized is lacking. Partial recovery also explains the different stress state observed following the PHR and PCR heat treatments. During the PCR anneal, the residual stress is fully relaxed during the time at temperature and the post-anneal residual stress is simply a function of the CTE mismatch. In contrast, the in-plane residual stresses in the PHR annealed sample have shifted toward tension during the anneal indicating that some relaxation of prior residual stress state occurred, but was not complete. In-situ annealing studies have been initiated to study the role of the initial microstructure on recover and recrystallization of the U-10Mo. The above information provides an opportunity to design a processing route to control the texture and microstructure of the U-10Mo foil, and thus the mechanical properties, by careful combinations of thermal and mechanical processing.

*Microstructural Evolution During Cladding* The microstructure of the U10-Mo foil clearly evolves during the HIP'ing step, which bonds the Al cladding to the foil at a temperature of 833K. The texture of neither the Zr diffusion barrier nor the U-10Mo foil evolves during HIP bonding. However, in the cases where a high dislocation density was present in the bare foil, it decreased significantly during bonding. That is to say, worked foils recovered during the bonding step, consistent with previous studies [9]. It is important to recognize that the strength of the U-10Mo fuel foil evolves throughout processing as evidenced by the changing dislocation density.

Here again, the importance of the stored energy in the microstructure as driver of recovery is evident. The $\varepsilon_{rms}$ of hot-rolled foil, which had a dislocation density of $11x10^{14}/m^2$, dropped modestly during the cladding. In contrast, the $\varepsilon_{rms}$ of the cold-rolled foils (20% and 50%), which had dislocation densities greater than $40x10^{14}/m^2$, decreased precipitously during the PCR anneal. The dislocation densities in the previously annealed bare foils did not change significantly following cladding. The residual stress in the U-10Mo foil, Zr diffusion barrier, and Al cladding following HIP bonding was dominated by the thermal mismatch of the constituent materials during cooling from the bonding. Little to no memory of the residual stresses prior to bonding is evident.

**Summary**

Neutron diffraction on the SMARTS diffractometer was used to monitor the evolution of residual stress, texture, and microstructure through seven processing steps of a U-10Mo foil roll bonded to a Zr diffusion prevention layer. The same foils were then HIP bonded to Al cladding and the diffraction measurements repeated. The thin foils made it impossible to use radial collimators to define the gauge volume as is traditionally done during residual stress measurements at white beam neutron sources. Rather, thin annealed Cu foils were symmetrically placed on the foils as an on-board calibrant. The calibration was demonstrably effective as shown by repeat measurements of the N lattice parameter in the opposing detector banks. However, it must be recalled that the diffraction measurements represent averages through the thickness of the U-10Mo foil and, where appropriate the Al cladding.

In the bare foil, the stresses in the U-10Mo are in the plane of the foil and moderate in magnitude, approaching 100MPa in tension following the highest temperature anneal. Correspondingly, the stresses in the much thinner Zr are large, exceeding -300MPa in the same instance. In the case of a heating step, the source of the stress is clear; the larger thermal expansion of the U-10Mo relative to the Zr results in a roughly equi-biaxial stress state in which the U-10Mo is in tension and the Zr in compression. The stress state following rolling is not so easy to understand and demands a finite element analysis to do so.

The crystallographic texture and dislocation density determined from the diffraction elucidate the evolution of the microstructure during the processing. Initial hot-rolling induces a relatively strong texture in the U-10Mo foil with (110) poles parallel to the rolling (L) direction and moderate dislocation density. The subsequent annealing at 923K for 45 minutes weakens the texture somewhat and reduces the dislocation density, but not to zero. Cold-rolling again strengthens the texture and increases the dislocation density to roughly four times that following hot-rolling. Following cold-rolling, a similar 923K anneal for 60 minutes completely randomizes the texture and reduced the dislocation density further than observed following the previous

anneal, indicating that recrystallization has occurred. The different microstructural results during the two annealing steps must be due to the difference in the microstructure entering the similar annealing processes. The increased dislocation density following cold working is indicative of higher stored energy in the microstructure with drives down the recovery and recrystallization temperatures. Annealing to 1023K and 1123K reduces the dislocation density further and a new texture, with (100) parallel to the rolling direction develops.

Following HIP bonding of the Al cladding to the different foils, the residual stresses changes completely, and shows little evidence of the different processing steps of the bare foils. In each case, the post-clad residual stresses in the U-10Mo fuel foil are predominantly in-plane compression, ~-150MPa in the L direction, -50MPa in the T direction. The Zr diffusion barrier is also under in-plane compression estimated to be -150MPa. Finally, the Al cladding experiences in-plane tension of ~50MPa in the L direction and less than 25MPa in the T direction. The HIP bonding of the cladding reduced the dislocation density in the rolled foils, but again the recovery depended on the amount of stored energy in the U-10Mo microstructure prior to bonding. That is, the cold-rolled foils exhibited a large reduction in dislocation density compared to the hot-rolled foils. Finally, the texture of the foils did not change during bonding, so that the final texture of the foil was completely determined by the processing of the foil.

These results provide controls with which the microstructure of the U-10Mo fuel foil can be designed to produce specific mechanical properties, be it a high flow strength, in-plane symmetry, etc.

**Acknowledgements**

This research was supported by the U.S. Department of Energy (DOE) and the National Nuclear Security Administration's Office of Global Threat Reduction through the DOE Idaho Operations Office Contract DE-AC07-05ID14517. The Lujan Center at the Los Alamos Neutron Science Center at LANSCE is funded by the U.S. DOE, Office of Basic Energy Sciences. Los Alamos National Laboratory is operated by Los Alamos National Security LLC under DOE Contract DE AC52 06NA25396.

| Sample ID | Hot Roll | PHR Anneal | Cold Roll | PCR Anneal |
|---|---|---|---|---|
| 490-1 | 90.5% | NA | NA | NA |
| 492-1 | 90.5% | 923 K, 45 min. | NA | NA |
| 493-1 | 88% | 923 K, 45 min. | 20% | NA |
| 482-1 | 81% | 923 K, 45 min. | 50% | NA |
| 485-1 | 81% | 923 K, 45 min. | 50% | 923 K, 60 min |
| 485-2 | 81% | 923 K, 45 min. | 50% | 1023 K, 60 min |
| 486-1 | 81% | 923 K, 45 min. | 50% | 1123 K, 60 min |

Table 1 Processing conditions for the samples studied in this work.

| U10Mo results | Hot-Rolled | 20% Cold-Rolled | 50% Cold-Rolled |
|---|---|---|---|
| $\langle X \rangle_A$ *(nm)* | 57 ± 7 | 52 ± 7 | 33 ± 5 |
| $\rho$ *($m^{-2}$)* | $(11 \pm 2)*10^{14}$ | $(43 \pm 4)*10^{14}$ | $(48 \pm 4)*10^{14}$ |
| *M (Wilkes arrangement parameter)* | 3 (fixed) | 3 (fixed) | 3 (fixed) |

Table 2 Parameters obtained from quantitative dislocation density of several of the samples studied in this work.

References


[1] J.L. Snelgrove, G.L. Hofman, M.K. Meyer, C.L. Trybus, T.C. Wiencek, Nuclear Engineering and Design, 187 (1997) 119-126.
[2] J.F. Jue, B.H. Park, C.R. Clark, G.A. Moore, D.D. Keiser, Nuc Tech, 172 (2010) 204-210.
[3] C.R. Clark, J.F. Jue, G.A. Moore, N.P. Hallinan, B.H. Park,in 28th International Meeting on Reduced Enrichment for Research and Test Reactors, Cape Town, South Africa, 2006.
[4] E. Perez, B. Yao, D.D. Keiser, Jr., Y.H. Sohn, J Nuc Matl, 402 (2010) 8-14.
[5] E. Perez, Y.H. Sohn, D.D. Keiser, Met. Trans. A, 44A (2013) 584-595.
[6] H. Palancher, A. Bonnin, C.V. Colin, V. Nassif, V. Honkimaki, R. Jungwirth, C. Ritter, G. Champion, Y. Calzavara, Powder Diffr, 28 (2013) S371-S393.
[7] G.K. Miller, D.E. Burkes, D.M. Wachs, Mater. Des., 31 (2010) 3234-3243.
[8] H. Ozaltun, M.H.H. Shen, P. Medvedev, J Nuc Matl, 419 (2011) 76-84.
[9] D.W. Brown, M.A. Okuniewski, J.D. Almer, L. Balogh, B. Clausen, J.S. Okasinski, B.H. Rabin, J Nuc Matl, 441 (2013) 252-261.
[10] G.A. Moore, B.L. Mackowiak, INL/EXT 13-29822, 2013,
[11] J. Crapps, K. Clarke, J. Katz, D.J. Alexander, B. Aikin, V.D. Vargas, J.D. Montalvo, D.E. Dombrowski, B. Mihaila, Nuclear Engineering and Design, 254 (2013) 43-52.
[12] M.A.M. Bourke, D.C. Dunand, E. Ustundag, App. Phys. A, A74 (2002) S1707-S1709.

[13] M.A.M. Bourke, J.A. Goldstone, T.M. Holden,in: M.T. Hutchings, A.D. Krawitz (Eds.) Measurement of Residual and Applied Stress Using Neutron Diffraction, Kluwer Academic Publishers, The Netherlands, 1992, pp. 369-382.
[14] A.D. Krawitz, Mater. Sci. Technol., 27 (2011) 589-603.
[15] D.W. Brown, T.M. Holden, B. Clausen, M.B. Prime, T.A. Sisneros, H. Swenson, J. Vaja, Acta. Mat., 59 (2011) 864-873.
[16] D.Q. Wang, X.L. Wang, J.L. Robertson, C.R. Hubbard, J. App. Crys., 33 (2000) 334-337.
[17] X.L. Wang, Y.D. Wang, J.W. Richardson, J. App. Crys., 35 (2002) 533-537.
[18] H. Ozaltun, P.G. Medvedev,in International Topical Meeting on Research Reactor Fuel Management, European Nuclear Society, Marakech, Morocco, 2010.
[19] H. Dolle, J. App. Crys., 12 (1979) 489-501.
[20] R.B. Vondreele, J.D. Jorgensen, C.G. Windsor, J. App. Crys., 15 (1982) 581-589.
[21] A.C. Larson, R.B. Von Dreele, Los Alamos National Lab 1986, Los Alamos, NM
[22] C.N. Tupper, D.W. Brown, R.D. Field, T.A. Sisneros, B. Clausen, Met. Trans. A, 43A (2012) 520-530.
[23] U.F. Kocks, C.N. Tome, H.R. Wenk, Texture and Anisotropy, Cambridge University Press, Cambridge, 1998.
[24] R.B. Von Dreele, J. App. Crys., 30 (1997) 517-525.
[25] B. Clausen, Los Alamos National Lab LA-UR 04-6581, 2004, Los Alamos, NM
[26] S. Vogel, D.W. Brown, M.A. Okuniewski, Los Alamos National Lab LAUR-10-05912, 2010, Los Alamos, NM
[27] I.C. Noyan, J.B. Cohen, Residual Stress-Measurement by Diffraction and Interpretation, Springer-Verlag, New York., 1987.
[28] J.E. Gates, E.G. Bodine, J.C. Bell, A.A. Bauer, G.D. Calkins, Batelle Memorial Institute BMI-APDA-638, 1958, Columbus, Oh
[29] A.M. Nomine, D. Bedere, D. Miannay,in J.J. Burke, D.A. Colling, A.E. Gorum, J. Greenspan (Eds.) Physical Metallugy of Uranium Alloys :Third Army Materials Technology Conference, Brook Hill Publishing Company, Vail, Colorado, 1974, pp. 657-700.
[30] D.W. Brown, D.J. Alexander, K.D. Clarke, B. Clausen, M.A. Okuniewski, T.A. Sisneros, Scripta Mat., 69 (2013) 666-669.
[31] S.R. Macewen, C. Tome, J. Faber, Acta. Met., 37 (1989) 979-989.
[32] D.W. Brown, T.A. Sisneros, B. Clausen, S. Abeln, M.A.M. Bourke, B.G. Smith, M.L. Steinzig, C.N. Tome, S.C. Vogel, Acta. Mat., 57 (2009) 972-979.
[33] H.E. Swanson, R.K. Fuyat, National Bureau of Standards (U.S.), 539 (1953) 1-65.
[34] J. Goldak, L.T. Lloyd, C.S. Barrett, Physical Review, 144 (1966) 478-484.
[35] R.B. Russell, JOM, 6 (1954) 1045-1052.
[36] D. Tromans, International Journal of Research and Reviews in Applied Sciences, 6 (2011) 462-483.
[37] G.K. Williamson, W.H. Hall, Acta Metall Mater, 1 (1953) 22-31.
[38] E.N. Aqua, Acta Crystallographica, 20 (1966) 560.
[39] M. Wilkens, Phys. Status Solidi A, 2 (1970) 359-370370.
[40] A. Leineweber, E.J. Mittemeijer, J. App. Crys., 43 (2010) 981-989.
[41] N.C. Halder, C.N.J. Wagner, Acta Crystallographica, 20 (1966) 312-&.
[42] T.H. De Keijser, E.J. Mittemeijer, H.C.F. Rozendaal, J. App. Crys., 16 (1983) 309-316.
[43] A.R. Stokes, A.J.C. Wilson, Proc. Phys. Soc, 56 (1944) 174-181.
[44] G. Ribarik, J. Gubicza, T. Ungar, Mat. Sci. Eng. A, 387 (2004) 343-347.

[45] T. Ungar, J. Gubicza, G. Ribarik, A. Borbely, J. App. Crys., 34 (2001) 298-310.
[46] D.W. Brown, M.A. Okuniewski, T.A. Sisneros, B. Clausen, G.A. Moore, Los Alamos National Lab LA-UR-14-22258, 2014, Los Alamos
[47] A. Rollett, F.J. Humphreys, Recrystallization and Related Annealing Phenomena, Elsevier Science, 2004.

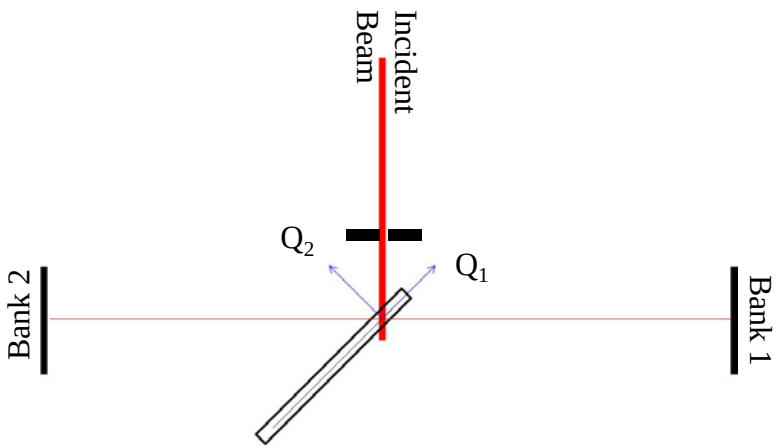


Figure 1. Schematic of the diffraction geometry of SMARTS indicating the diffraction vectors of each detector bank. The samples are shown as mounted to determine the lattice parameters in the T and N sample directions of the mini plates in banks 1 and 2, respectively. Bank 3 lies below the incident neutron beam at a scattering angle of 148$^{o}$.

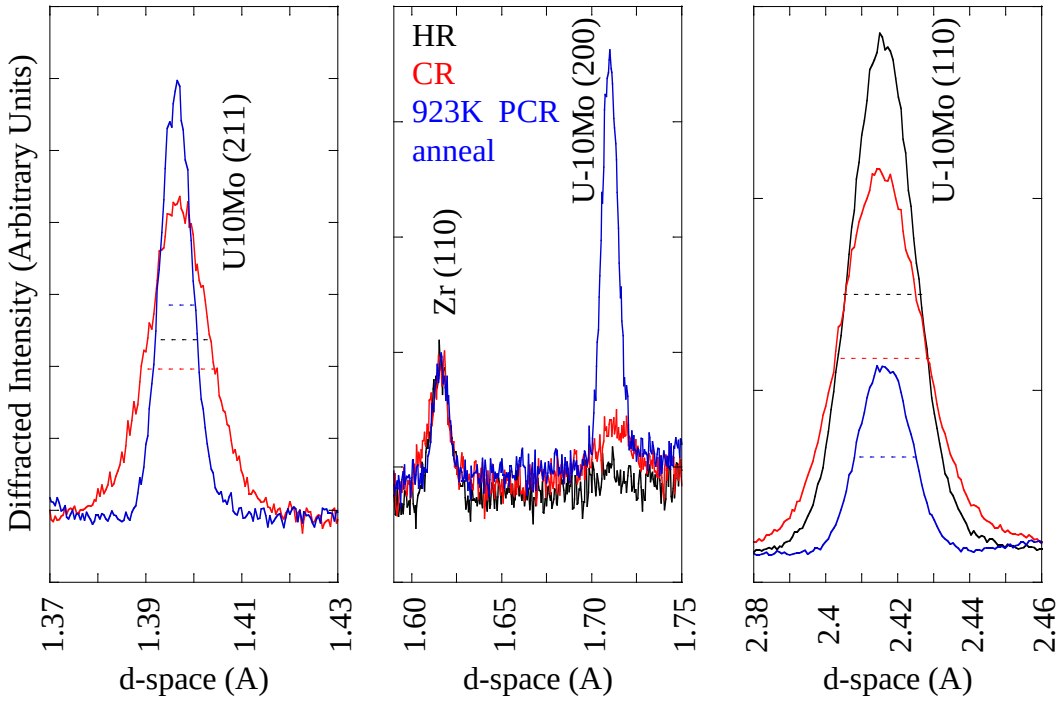


Figure 2. Sections of diffraction patterns from the hot-rolled (black), 50% cold-rolled (red), and 923K PCR annealed (blue) samples highlighting the U10-Mo (110), (200), and (211) peaks as well as the Zr (110) peak. The dashed lines indicate the FWHM of each peak.

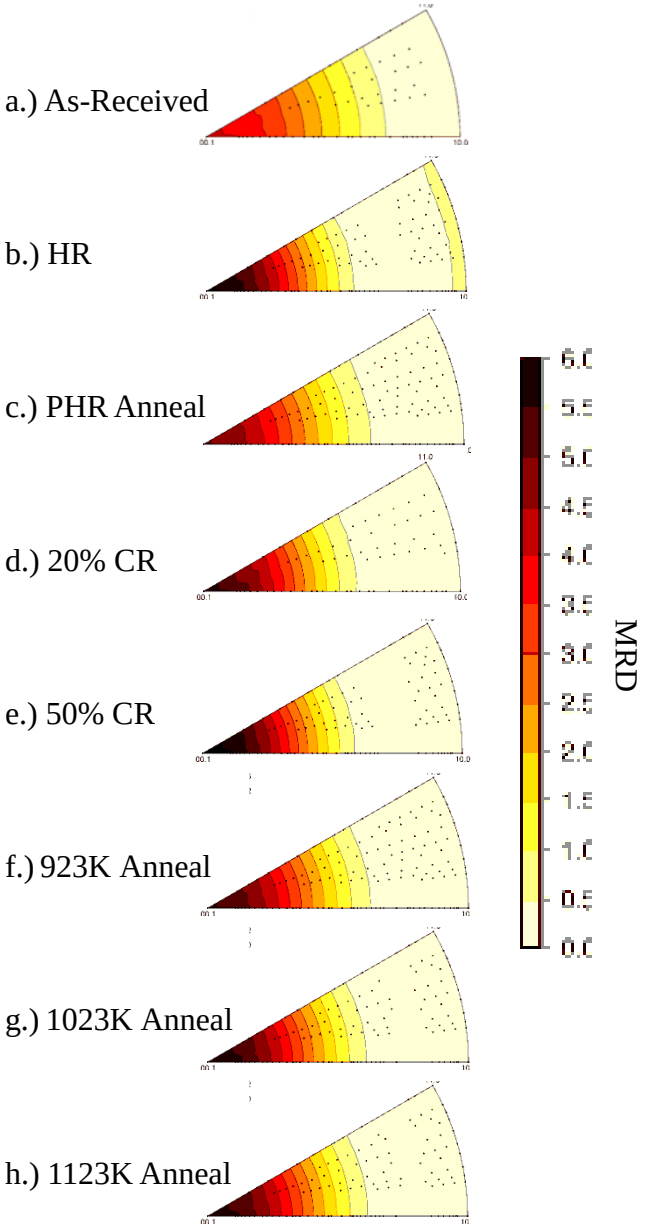


Figure 3. N direction IPF representing texture of the Zr diffusion prevention layer. Contours go from 0 to 6 MRD at intervals of 0.5 MRD.

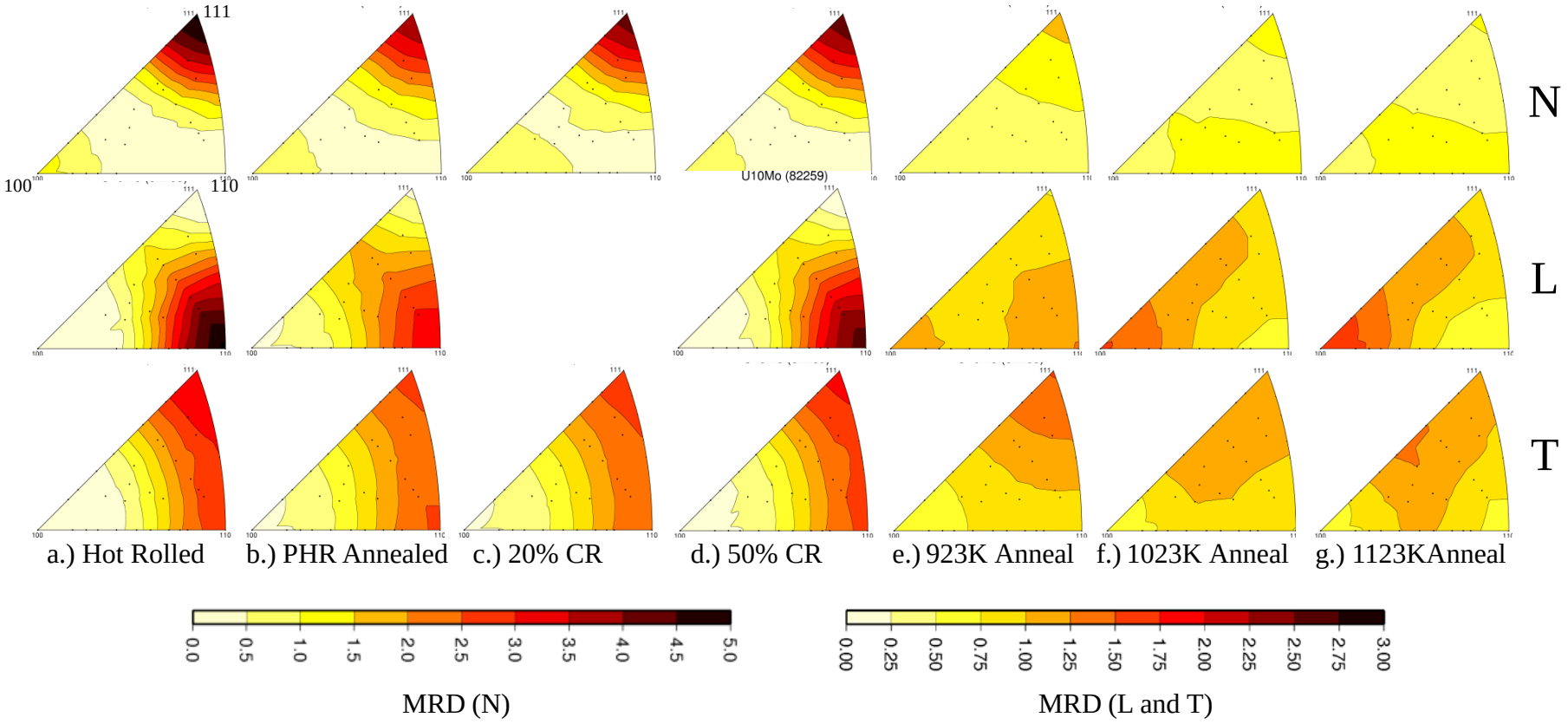


Figure 4. IPF's representing texture in the center of the bare U10Mo foils as a function of last processing step. Contours on N direction IPF's go from 0 to 5 MRD at intervals of 0.5MRD. Contours on L and T direction IPF's go from 0 to 3 MRD at intervals of 0.25MRD.

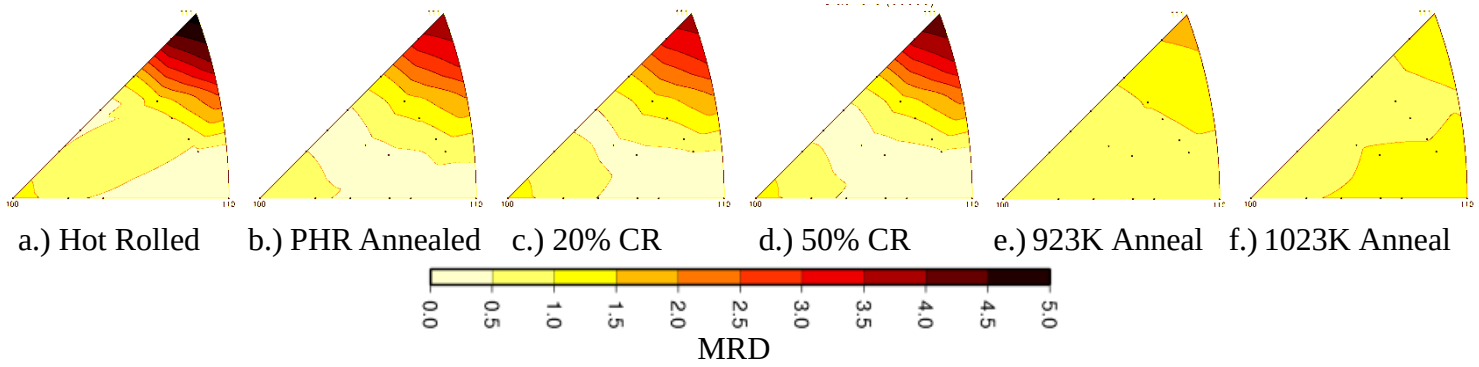


Figure 5. N direction IPF representing texture in the center of the clad U10Mo foils as a function of last processing step prior to HIP bonding. Contours go from 0 to 5 MRD at intervals of 0.5MRD.

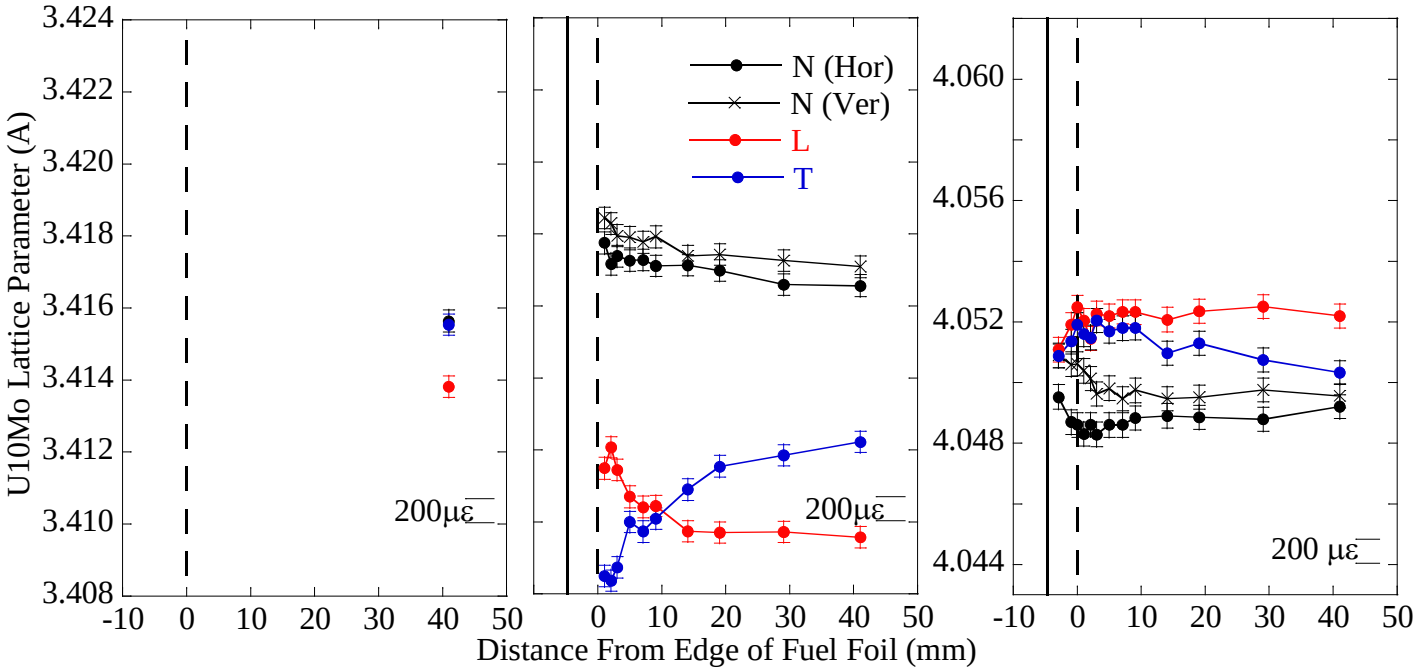


Figure 6. U10Mo lattice parameters measured in the three sample directions in the hot-rolled foil, 490-1 as a function of distance from the end of the foil on the a.) bare foil and b.) following cladding. c.) Al lattice parameter measured in the cladding. Open and closed symbols represent repeat measurements of the normal direction lattice parameter with the sample vertical and horizontal respectively.

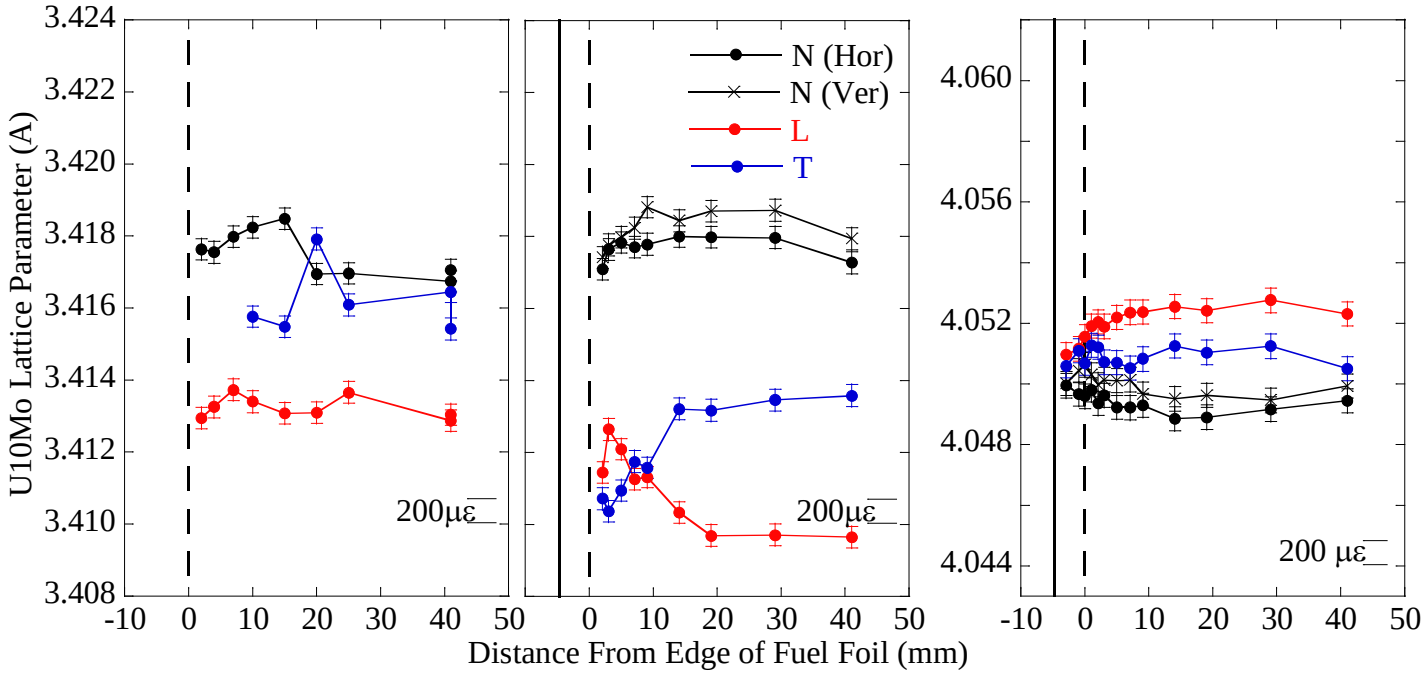


Figure 7. U10Mo lattice parameters measured in the three sample directions in the cold-rolled foil, 482-1 as a function of distance from the end of the foil on the a.) bare foil and b.) following cladding. c.) Al lattice parameter measured in the cladding. Open and closed symbols represent repeat measurements of the normal direction lattice parameter with the sample vertical and horizontal respectively.

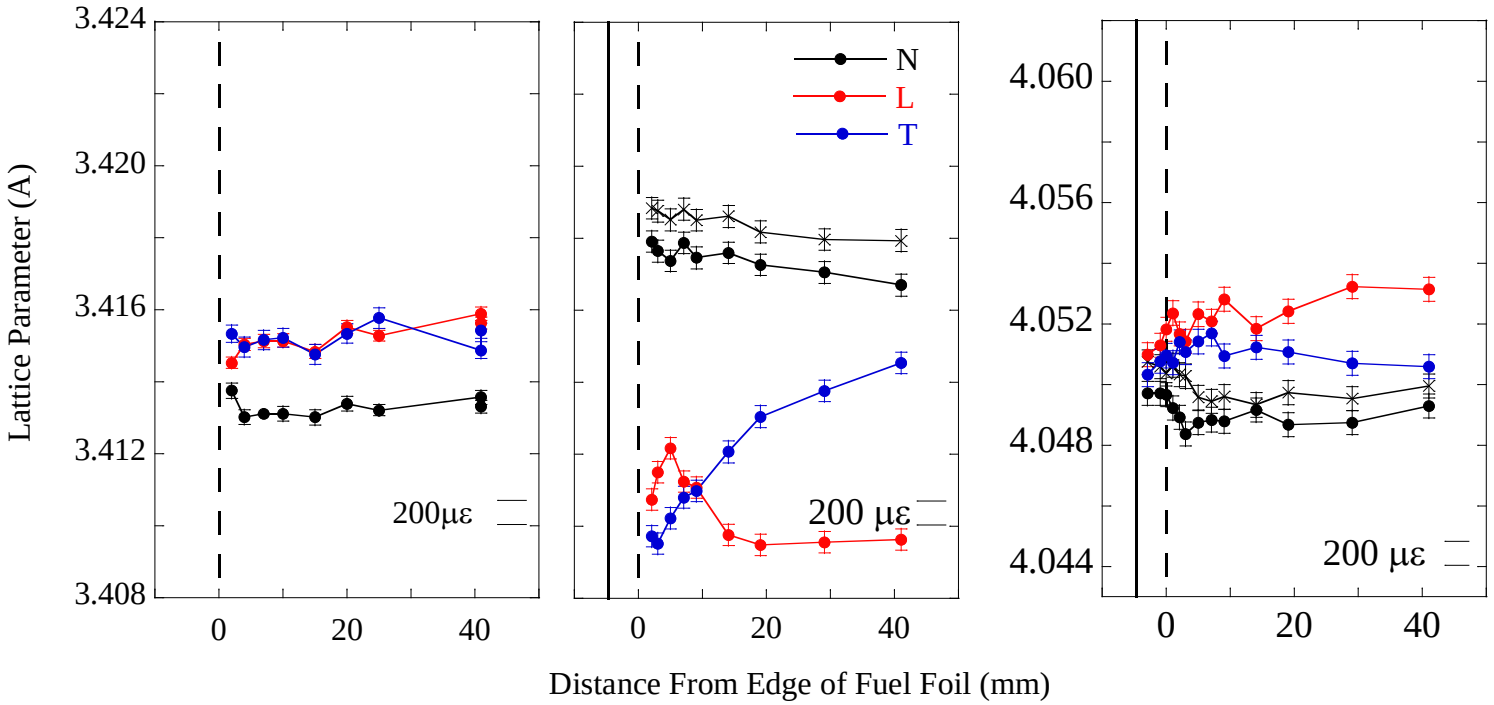


Figure 8. U10Mo lattice parameters measured in the three sample directions in the PCR annealed at 823K sample, 485-1 as a function of distance from the end of the foil on the a.) bare foil and b.) following cladding. c.) Al lattice parameter measured in the cladding. Open and closed symbols represent repeat measurements of the normal direction lattice parameter with the sample vertical and horizontal respectively.

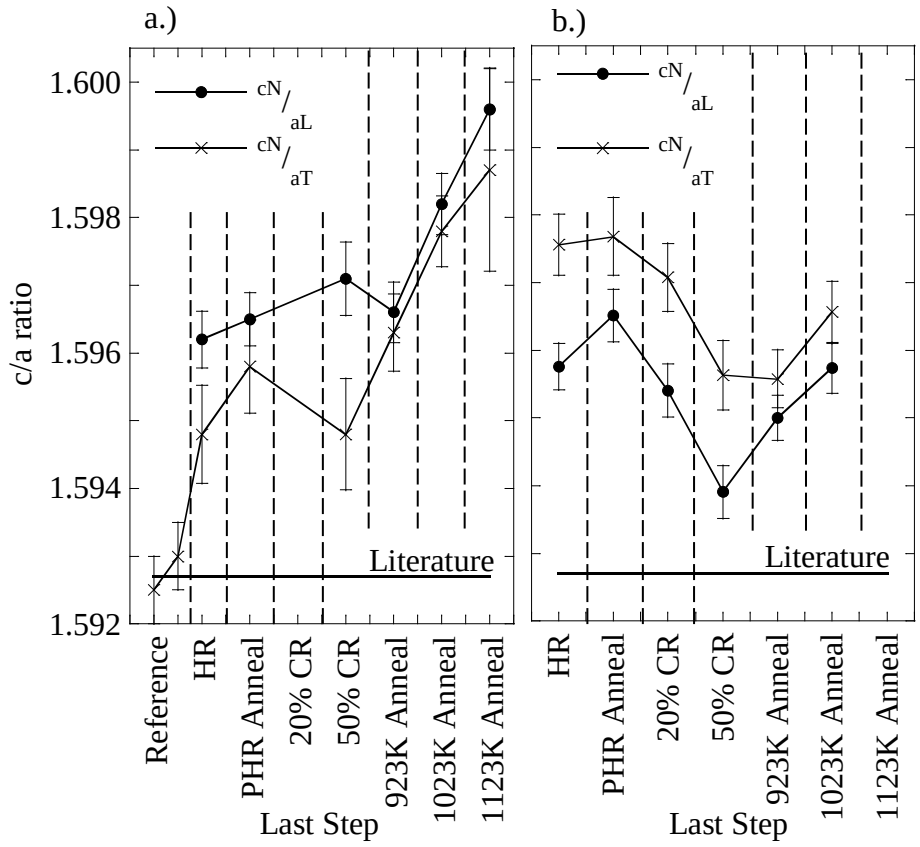


Figure 9a.) Zr c/a ratios in the center reference Zr and center of each bare U-10Mo foil, as a function of final processing step presented chronologically. b.) same in the clad plates.

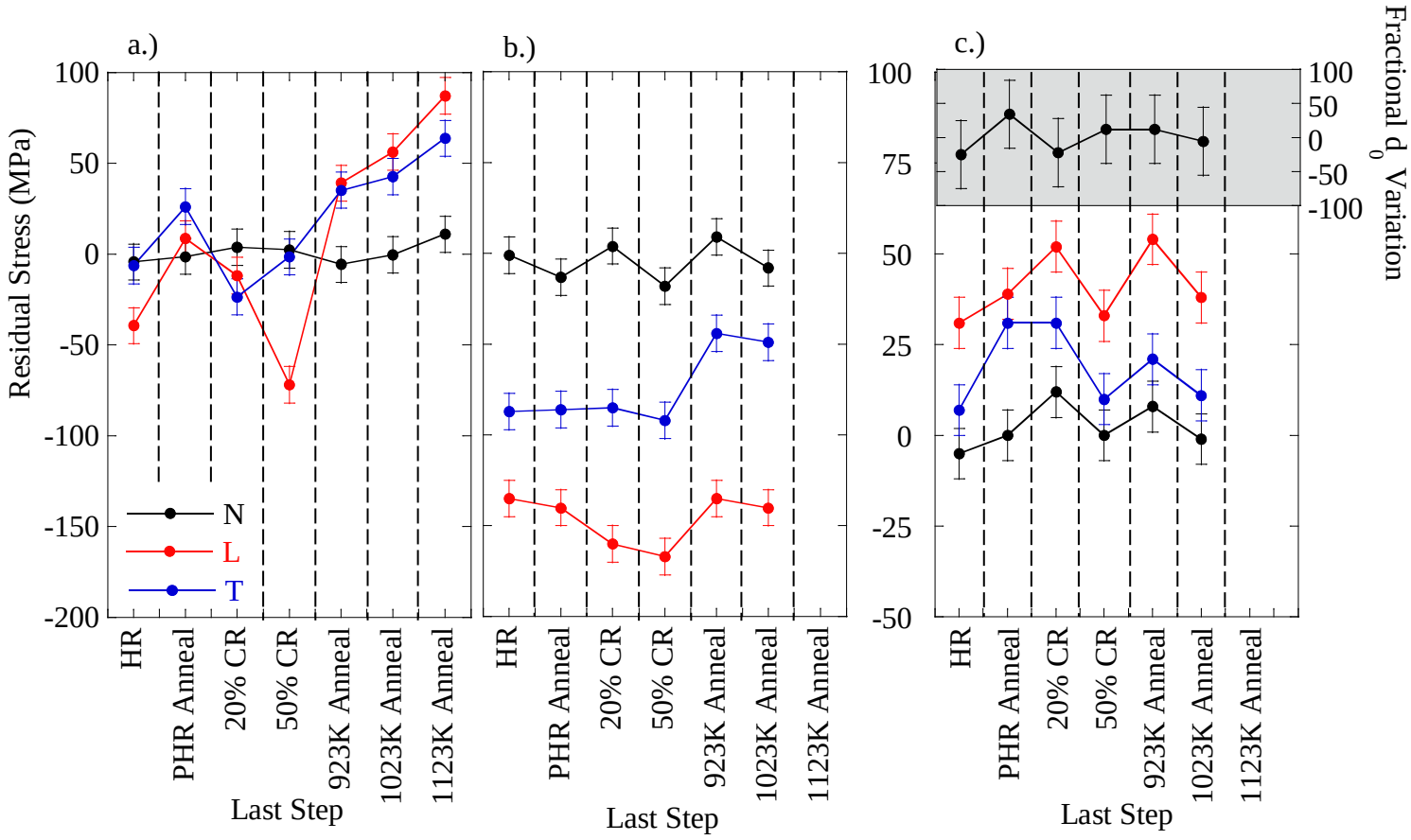


Figure 10.) N, L, and T stress components in theU-10Mo fuel in the a.) bare foil, b.) clad plate, and c.) in the Al cladding in the clad plate as a function of the last processing step of the bare foil. The shaded inset shows the fractional variation of the Al reference lattice parameter, $d_0$, ($x10^6$) found by forcing the normal component of the Al stress to zero.

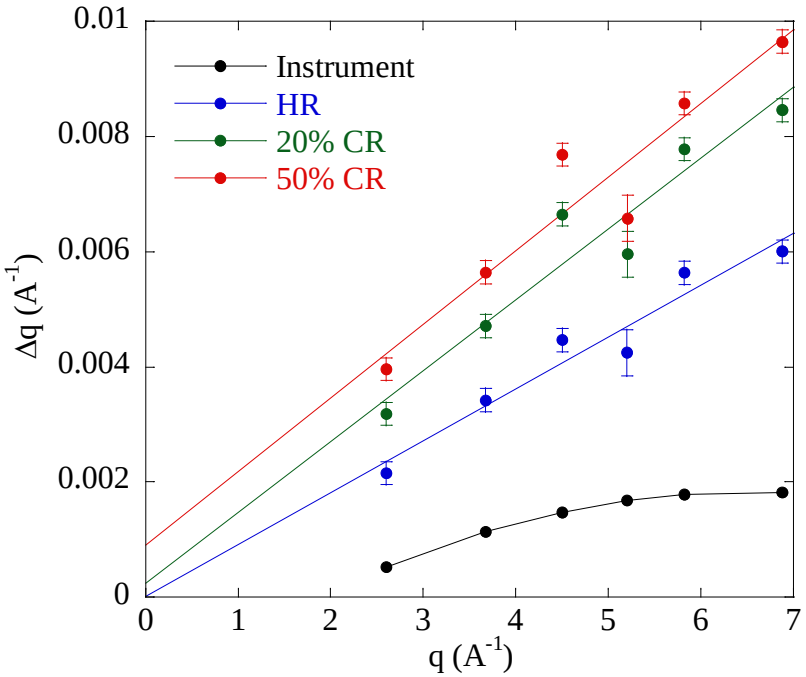


Figure 11. Conventional Williamson-Hall plot of the peak breadth in momentum transfer vs. momentum transfer.

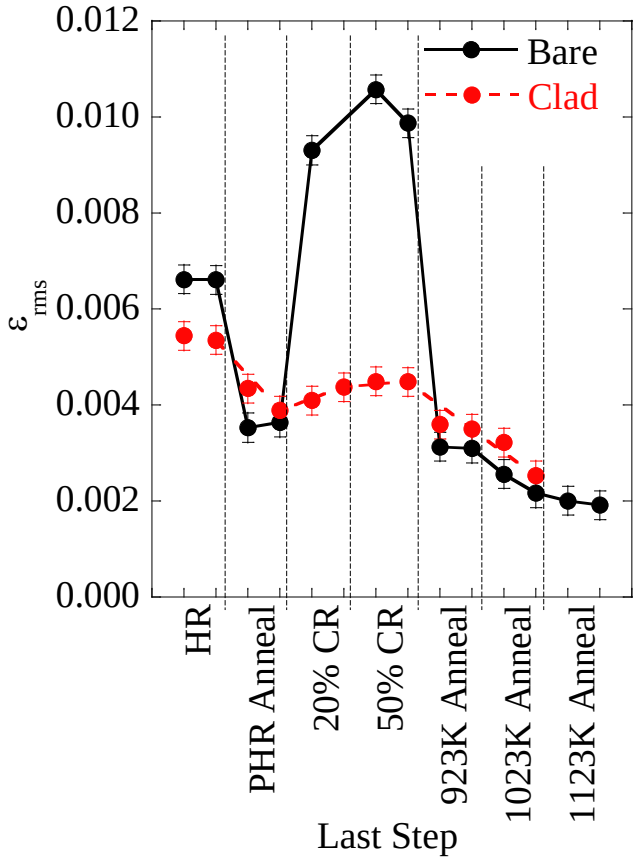


Figure 12. Root mean square strain in U-10Mo fuel in the bare foil (•) and clad plate (x) as a function of final processing step of the bare foil.